RSC Advances

ROYAL SOCIETY OF CHEMISTRY

www.rsc.org/advances

RSC Advances

RSCPublishing

COMMUNICATION

Stabilization of Silicon Nanoparticles in Graphene Aerogel Framework for Lithium Ion Storage

Cite this: DOI: 10.1039/x0xx00000x

Binghui Xu,[a] Hao Wu,[a] C. X. (Cynthia) Lin,[a] Bo Wang,[a,b] Zhi Zhang,[c] and X. S. Zhao[a]*

Received ooth January 2012,
Accepted ooth January 2012

DOI: 10.1039/x0xx00000x

www.rsc.org/

The severe volume change and aggregation of silicon nanoparticles (SiNPs) when used as an anode for lithium ion batteries (LIBs) are the key issue. Here, we demonstrate a novel approach to wrapping SiNPs in three-dimensional reduced graphene oxide (RGO) aerogel. The RGO aerogel not only provides a porous network for entrapping SiNPs to accommodate the volume change during cycling, but also facilitates electrolyte transport. Furthermore, the continuous RGO network is favourable for electron transfer. The graphene-wrapped SiNPs were stable and displayed an excellent rate capacity, delivering a reversible capacity of about 2000 mA h g^{-1} after 40 cycles.

Introduction

With the fast growing demands for energy storage devices, the development of new-generation LIBs is becoming increasingly important. Achieving high capacity, excellent cycling performance and rate capability with innovative electrode materials has been one of the main challenges. [1] Silicon (Si) is a promising anode material for new-generation LIBs because of its high theoretical Li ion storage capacity (~4200 mAh·g^{-1}), significantly higher than that of commercialized graphite (372 mAh·g^{-1}). Si also features low discharge potential (~0.4 V vs Li/Li^+), rich natural abundance, and environmental benignity. [2-4] However, the realization of Si as a LIB anode has been hindered because Si suffers from not only a low intrinsic electronic conductivity but also a large specific volume changes (>300%) during lithiation and delithiation, resulting in pulverization of Si particles and electrical disconnection from the current collector, leading to a rapid capacity fading. [5-7] To solve these problems, nanostructured Si electrodes such as nanoparticles [4, 8-10], nanowires [11-15], nanotubes and hollow spheres [16, 17] have been explored. Combining SiNPs with carbon materials has also been studied. [8, 10, 18-23]

Graphene, a monolayer of carbon atoms arranged in a two-dimensional (2D) honeycomb network, has been used to improve the stability and electric conductivity of nanostructured Si electrodes for LIBs. [24] Due to its high electronic conductivity, superior mechanical strength and flexibility, graphene can improve electron transport and Li^+ diffusion, thus enhancing the electrochemical performance of SiNPs for lithium ion storage. [23, 25-27] In spite of the observed improvement of the electrochemical performance of SiNPs by graphene, SiNPs still tend to aggregate. As a result, the performance of the graphene-SiNPs composites inevitably degrades during charge/discharge. Recently, three-dimensional (3D) graphene materials, including hydrogels and aerogels, have been shown to possess advantages, such as high surface area and good electrical conductivity. [28-30] These 3D graphene materials may be favourable for stabilizing SiNPs.

This paper describes a method for preparing graphene-stabilized SiNPs on the basis of electrostatic interactions. Because both graphene oxide (GO) and SiNPs (there is a thin layer of SiO_2 on the surface of the SiNPs) are negatively charged in a wide pH range, the SiNPs used in this work were firstly modified using poly(diallydimethylammonium chloride) (PDDA, a positively charged polyelectrolyte) to change the surface charge nature from being negative to being positive following a protocol described elsewhere. [23] As schematically illustrated in Scheme 1, the PDDA-modified SiNPs interacted strongly with negatively charged GO sheets to form a Si-GO composite (hereinafter designated as Si@GO). Because of the flexibility of GO sheets, SiNPs were wrapped in by the GO sheets. The GO in the Si@GO suspension was then reduced using gallic acid (GA, a natural plant phenolic acid; see Figure S1A for its structure) in an oil bath at 95 °C for 4 h. It has been reported that in the presence of natural phenolic acid, GO can be reduced to assemble into RGO hydrogels driven by the enhancing

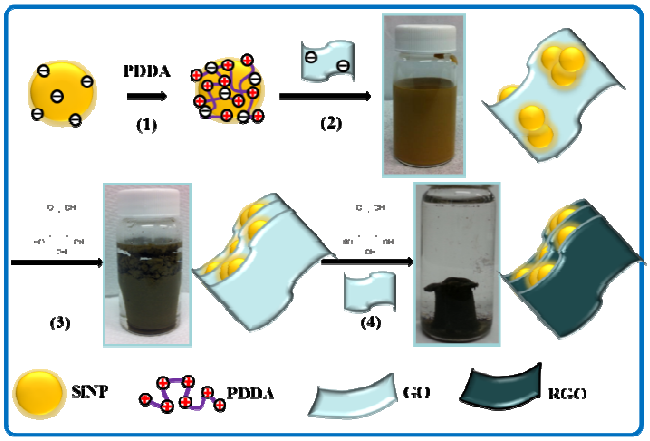

Scheme 1. Schematic illustration of the preparation of Si/RGO-AG: 1) surface modification of SiNPs with PDDA; 2) formation of Si@GO composite via electrostatic interactions; 3) reduction of Si@GO using GA to form Si@RGO hydrogel; 4) dispersing Si@RGO in a GO suspension for further reduction using GA.

hydrophobicity and π–π interactions among the nanosheets during the reduction. [28, 31] During this GA reduction process, yellow-brown-coloured Si@GO suspension gradually turned transparent to form a dark grey gel separating from the suspension, indicating that the GO had been reduced to reduced graphene oxide (RGO) and the SiNPs had been wrapped by the RGO architecture. In order to understand the stabilization effect of RGO sheets on SiNPs, the obtained Si@RGO hydrogel was crushed and redispersed in an aqueous GO suspension, which was further reduced with GA at 95 °C for 12 h. After freeze-drying and thermal reduction at 700 °C for 2 h under H_2/Ar atmosphere, a black 3D RGO aerogel with confined SiNPs, designated as Si/RGO-AG, was obtained. For comparison purpose, another two samples were prepared. One of them, designated as Si/RGO, was prepared by mixing SiNPs with aqueous GO suspension, followed by filtration and thermal reduction at 700 °C for 2 h under H_2/Ar atmosphere. The other one, designated as Si/RGO-SWAG (SiNPs were wrapped by RGO aerogel in a single step), was prepared according to the same procedure of preparing sample Si/RGO-AG except for without Step 3 (see Scheme 1).

Experimental Section

Preparations of graphene oxide (GO)

The GO used in this work was prepared from natural graphite flake (Sigma Aldrich, 325 mesh) by using a modified Hummers method.[32]

Preparation of RGO aerogel wrapped SiNPs (Si/RGO-AG)

SiNPs (120 mg, 99% purity, from Nanostructured & Amorphous Materials, Inc.) and 20wt% PDDA (3.0 g, Sigma Aldrich, MW = 10000-20000) aqueous solution were dispersed in water (120 mL) under sonication in a water bath (KQ3200DE, 40 kHz). Excess PDDA was washed away by centrifugation (10000 rpm) four times, followed by vacuum drying. An aqueous GO suspension (15 mL, 2 mg·mL^{-1}) was centrifuged at 5000 rpm for 30 min to remove any graphite particles and then mixed with the above PDDA-modified SiNPs (120 mg) under sonication for 1 h. After the addition of GA (13 mg), the mixed suspension was transferred to a 20 mL capped vial and placed into an oil bath at 95 °C for 4 h to form a Si@GO hydrogel. The hydrogel was collected and redispersed in another GO aqueous suspension (15 mL, 2 mg·mL^{-1}) and GA (13 mg) under sonication. The suspension was then transferred into a 20 mL vial to prepare hydrogel at 95 °C for 12 h. The resulting hydrogel monolith was soaked in distilled water, followed by freeze-drying. Reduction was conducted in a quartz tube at 700 °C for 2 h under a H_2/Ar (5:95 v/v) atmosphere with a heating rate of 2 °C min^{-1} to obtain sample Si/RGO-AG.

Preparation of other samples

For comparison purpose, another two samples were prepared. One of them, designated as Si/RGO, was prepared as follows. An aqueous GO suspension (30 mL, 2 mg·mL^{-1}) was mixed with PDDA-modified SiNPs (120 mg) under sonication for 1 h. After the addition of GA (26 mg), the suspension was reduced at 95 °C in an oil bath for 12 h under magnetic stirring. Then the solid was collected by filtration, followed by vacuum drying and reduction in a quartz tube at 700 °C for 2 h under a H_2/Ar (5:95 v/v) atmosphere with a heating rate of 2 °C min^{-1}. The other sample, designated as Si/RGO-SWAG, was prepared as follows. An aqueous GO suspension (15 mL, 2 mg·mL^{-1}) was mixed with PDDA-modified SiNPs (60 mg) under sonication for 1 h. After the addition of GA (13 mg), the suspension was transferred into a 20 mL capped vial and placed in an oil bath at 95 °C for 12 h. The resulting hydrogel monolith was soaked in distilled water, followed by freeze-drying. Reduction was conducted in a quartz tube at 700 °C for 2 h under an H_2/Ar (5:95 v/v) atmosphere with a heating rate of 2 °C min^{-1}.

Characterization

The TEM and HRTEM measurement was performed on a Philips Tecnai F20 and Philips Tecnai F30 field emission transmission electron microscopes operated at 200 kV. SEM images were obtained from a JEOL 7800F scanning electron microscope operated at 5.0 kV. XRD patterns were collected on a German Bruker D8 Advanced X-Ray Diffractometer with Ni filtered Cu Kα radiation (40 kV, 30 mA). Thermo gravimetric analysis (TGA) was carried out on a TGA/DSC1 STAR^e System under air flow (25-900 ºC, 5 ºC/min). X-ray photoelectron spectra (XPS) were collected on a Kratos Axis ULTRA X-ray photoelectron spectrometer using a monochromatic Al Ka (1486.6 eV) X-ray source and a 165 mm hemispherical electron energy analyzer. Nitrogen physisorption isotherms were measured at 77 K on Tristar II 3020. All samples were degassed at 200 °C for 12 h prior to the measurements. The specific surface areas of the samples were calculated using the Brunauer–Emmett–Teller (BET) method and the total pore volumes were estimated from the nitrogen volumes adsorbed at the relative pressure of 0.99. The pore size distribution curves were derived from the Barrett-Joyner-Halenda (BJH) method of isotherm analysis. Raman spectra were collected on a Thermo-Fischer Almega dispersive Raman instrument. The instrument was fitted with both 633 and 785 nm lasers. Energy-dispersive X-ray spectroscopy analysis (EDX) was conducted on a JSM6610 EDS system.

Electrochemical measurements

The electrochemical properties of the prepared samples were evaluated with CR2032 coin cells. The electrodes were prepared by mixing the active materials with conductive carbon black (Super-P) and poly(vinylidene fluoride) (PVDF) dissolved in N-methyl-2-pyrrolidone (NMP) with a mass ratio of 80:10:10 to form a homogeneous slurry under magnetic stirring. The slurry was then spread onto a pure Cu foil. Pure lithium metal discs were selected as

the counter electrode. The electrolyte used was 1 M $LiPF_6$ in ethylene carbonate/dimethyl carbonate (1:1 v/v). A Celgard 2400 microporous polypropylene membrane was used as the separator. The CR2032 cells were assembled in an argon-filled glove box (Mbraun Unilab) with water and oxygen contents less than 1 ppm. Cyclic voltammetry was carried out on a CHI 660D electrochemical workstation at a scan rate of 0.1 $mV \cdot s^{-1}$. The discharge and charge measurements of the batteries were performed on a Neware system in the fixed voltage window between 0.02 and 1.2 V at room temperature.

Results and discussion

The morphology and microstructure of the Si/RGO-AG composite were characterized using scanning electron microscopy (SEM), transmission electron microscopy (TEM) and high-resolution TEM (HRTEM) techniques. The HRTEM image in Figure S1B shows that there was a shell around the SiNPs with a thickness of about 5 nm. The X-ray photoelectron spectroscopy (XPS) results of the SiNPs in Figure S2 shows a peak at 103 eV, which is attributed to Si 2p electrons in Si-O_4, [33] confirming the shell was silicon oxide (SiO_2). This SiO_2 layer plays a vital role in modifying the surface chemistry of SiNPs. [23] The silanol groups on the surface of the SiO_2 shell can be ionized under the experimental conditions to carry a negative charge, thus enabling strong electrostatic interactions between the SiNPs and PDDA to change the SiNPs from a negatively charged surface to a positively charged surface. On the other hand, according to a recent study, [34] the SiO_2 layer can suppress the volume expansion of SiNPs although it consumes some lithium ions during the first discharge cycle.

Figures 1A and 1B are the SEM images of Si/RGO-AG under different magnifications. SiNPs with an average diameter of 100 nm dispersed the 3D RGO aerogel framework can be clearly seen. On contrast, severe aggregation of SiNPs can be observed from pure SiNPs (Figure S3A), sample Si/RGO (Figure S3B) and sample Si/RGO-SWAG (Figure S3C, S3D). In particular, the SiNPs in sample Si/RGO formed micro-sized aggregates. After a single-step wrapping by RGO, the aggregation of SiNPs was not significant. However, some SiNPs were not fully wrapped by RGO and aggregates can be still observed. This explains the capacity fading of sample Si/RGO-SWAG. The elemental analysis results of Si/RGO-AG (Figure S4) confirmed the existence of major elements Si and C and their homogeneous distribution in the 3D aerogel. In this Si/RGO-AG composite, the graphene aerogel provides a porous network for the entrapped SiNPs, thus is beneficial for accommodating the volume change of these SiNPs during electrochemical reactions. The porous network also facilitates electrolyte transport, potentially enhancing the rate capacity of LIBs. Besides, the continuous interconnected graphene network creates favourable electron pathways against cycling processes. The

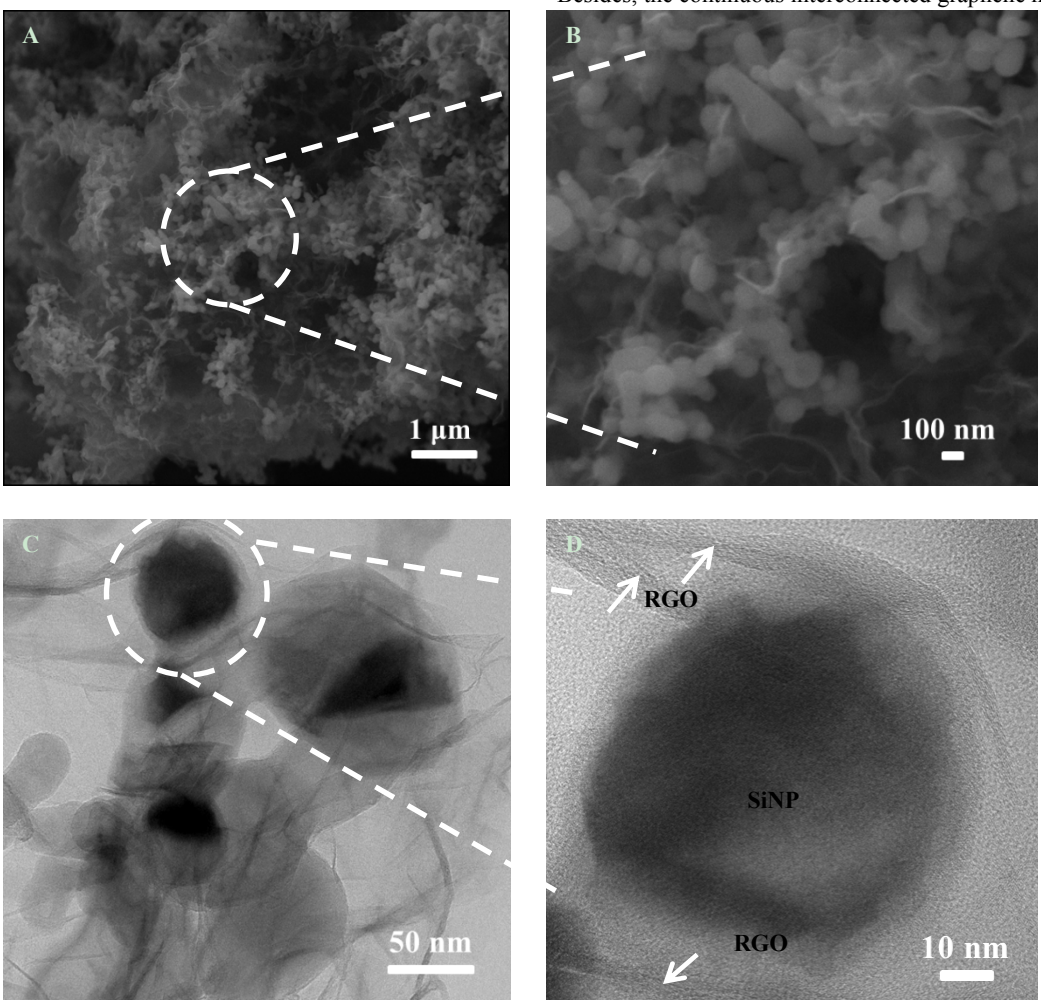

Figure 1. SEM (A, B), TEM (C), and HRTEM images (D) of Si/RGO-AG composite.

HRTEM image shown in Figure 1C also clearly demonstrates the existence of a continuous RGO network with SiNPs entrapped. The HRTEM image in Figure 1D shows that SiNPs were well-encapsulated within the RGO aerogel network.

Figure 2A shows the X-ray diffraction (XRD) patterns of Si/RGO-AG and SiNPs. All diffraction peaks due to SiNPs can be seen from sample Si/RGO-AG, indicating that the silicon crystalline structure in the Si/RGO-AG composite retained after the freeze-drying and thermal reduction treatments. Figure 2B presents the Raman spectra of Si/RGO-AG and pristine SiNPs. The absorption bands due to SiNPs can be seen from Si/RGO-AG, confirming the presence of crystalline Si particles in the composite. There are two more absorption bands at 1350 and 1596 cm^{-1}, respectively. These two peaks are assigned to the D band and G band of graphene, respectively, [35] confirming the presence of RGO in the composite.

Figure S5 presents the C1s XPS spectra of samples. As can be seen, GO showed three peaks at 284.9, 286.8, and 289.0 eV, corresponding to C=C in aromatic rings, C-O-C in epoxy and alkoxy, and C=O in carbonyl and carboxyl groups, respectively. It is clearly seen that the peak intensity due to C-O-C and C=O bonds of sample Si/RGO-AG is significantly lower than that of sample GO. The intensity of the peak ascribed to C=C however increased after reduction. These data suggest that the oxygen-containing groups on GO were largely removed, and most of the conjugated bonds were restored by GA reduction and thermal treatment.

The N_2 adsorption/desorption isotherms of the Si/RGO-AG composite (see Figure 2C) showed a type IV isotherm with an H_3 hysteresis loop, indicating a mesoporous structure of the material. The Brunauer-Emmett-Teller (BET) surface area and pore volume of the composite was measured to be 125 m^2/g and 0.37 cm^3/g, respectively, much higher than that of pure SiNPs (25 m^2/g and 0.055 cm^3/g, respectively, see Figure S6A). The Barrett-Joyner-Halenda (BJH) pore size distribution curve of Si/RGO-AG (see Figure 2D) demonstrates that Si/RGO-AG composite had a mesoporous structure with two pore systems. The intensive peak around 5.0 nm is due to the presence of small gaps among randomly stacked graphene sheets, while the broad peak centred at about 26 nm may be due to the large voids between inter-twisted graphene sheets [36]. The high surface area along with the existence of mesopores in Si/RGO-AG should offer a large material-electrolyte contact area and promote the diffusion of Li^+ ions if Si/RGO-AG is used as electrode materials for lithium storage.

Thermal gravimetric analysis (TGA) was carried out in air and the results are shown in Figure S6B. It can be seen that the mass of the pristine SiNPs increased slightly with a mass gain of about 0.150 wt% at 700 °C. This gain was due to the oxidation of Si by O_2 to form SiO_2. At 700 °C, the residual of the RGO aerogel was about 3.02 wt%, which was due to the impurities in the GO sample. The weight loss of the Si/RGO-AG composite at 700 °C was about 19.3 wt%. Based on the TGA data, the Si/RGO-AG composite was calculated to contain about 80.0 wt% SiNPs and 20.0 wt % RGO aerogel.

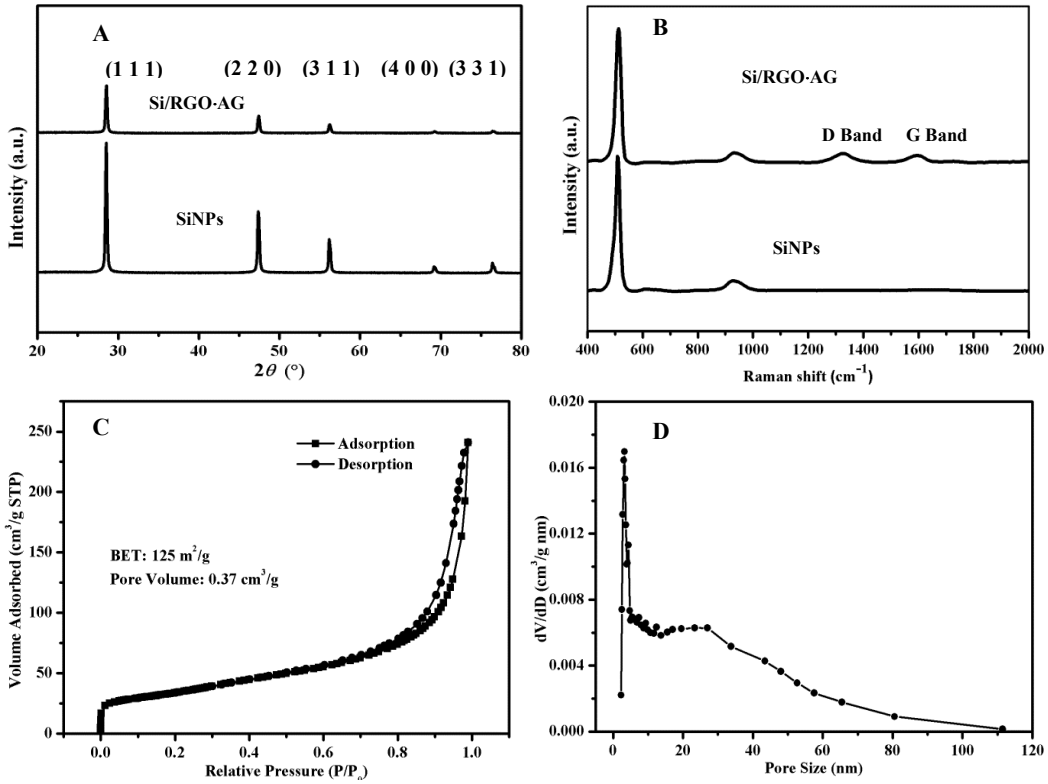

Figure 2. XRD patterns of SiNPs and Si/RGO-AG (A); Raman spectra of SiNPs and Si/RGO-AG (B); N2 adsorption/desorption isotherms (C) and BJH pore size distribution based on desorption isotherm of Si/RGO-AG (D).

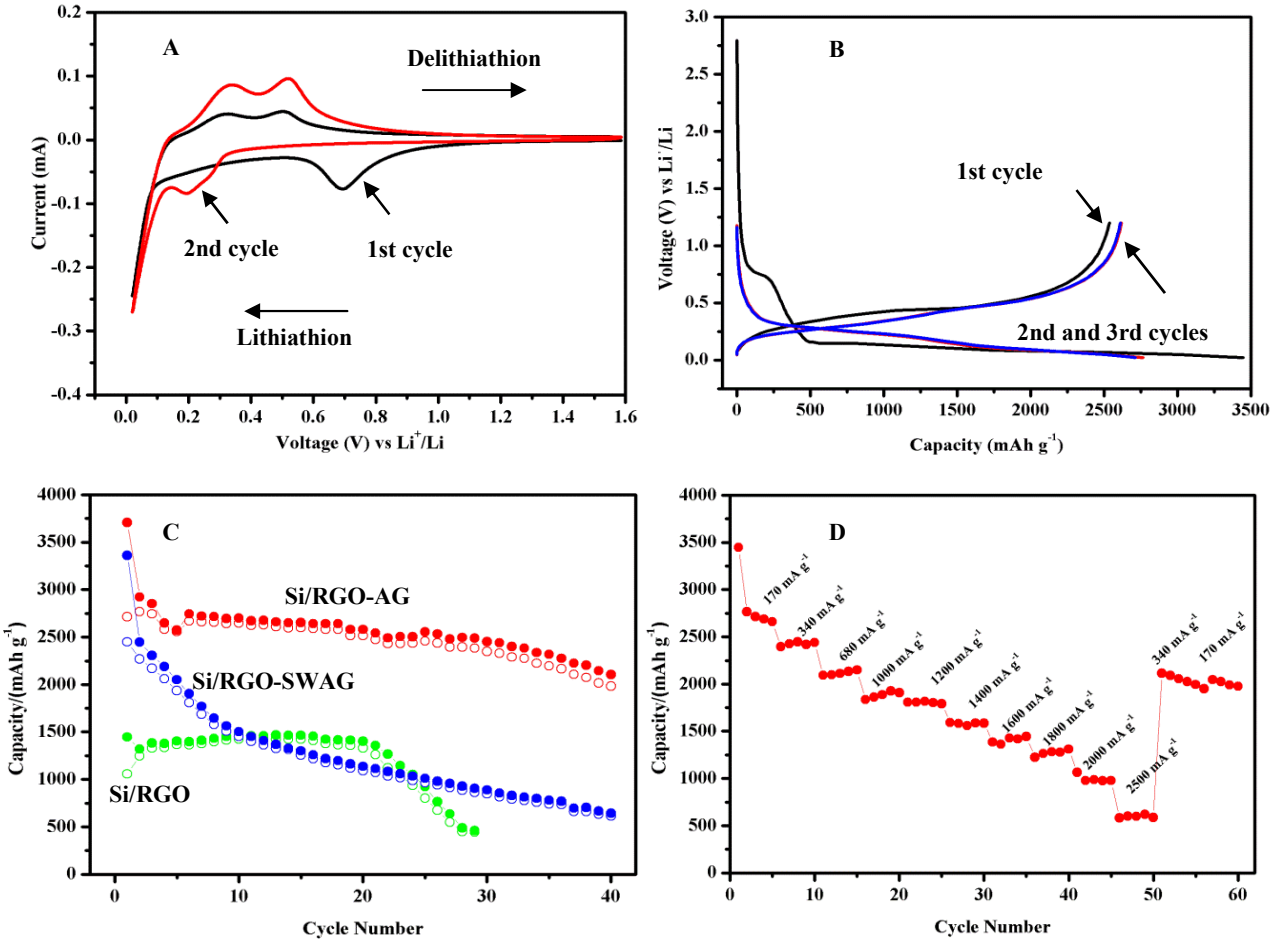

Figure 3. (A) Cyclic voltammetry curves for Si/RGO-AG for the first two cycles; (B) Galvanostatic discharge/charge profiles of the first three cycles; (C) cycling performance of electrode Si/RGO-AG, Si/RGO-SWAG, and Si/RGO; (D) rate capability of electrode Si/RGO-AG.

The electrochemical performance of the Si/RGO-AG composite as an anode was assembled and tested in a CR2032 coin cell where lithium foil was used as a counter electrode. For comparison, the cycling performance of electrode Si/RGO was also tested under the same experimental conditions. Figure 3A shows typical cyclic voltammetry (CV) curves of electrode Si/RGO-AG in the potential range of 0.02-1.20 V (vs Li^+/Li) at a scan rate of 0.1 $mV \cdot s^{-1}$ of the first two cycles, starting at the open circuit potential of 1.59 V. A broad cathodic peak in the first cycle appeared at 0.69 V, indicating the formation of solid electrolyte interphase (SEI). [8] This cathodic peak disappeared in the second cycle and correlated to an initial capacity loss. The main cathodic part of the second cycle displayed a peak at 0.19 V, corresponding to the formation of Li-Si alloy phases [37]. The anodic part showed two peaks at 0.34 and 0.52 V, corresponding to the phase transition from Li-Si alloys to amorphous Si. [8, 23]

Figure 3B displays the discharge/charge profiles of the initial three cycles of electrode Si/RGO-AG under a current density of 150 $mA \cdot g^{-1}$ in the voltage window of 0.02 to 1.2 V (vs. Li^+/Li). The onset slope at about 0.7 V in the initial discharging curve, which disappeared in the following cycles, corresponds to the SEI formation. [8] Besides, the main discharge plateau is around 0.2 V and the charge plateau is around 0.5 V. All these features are in good agreement with the CV results discussed above. The specific capacity was calculated based on the total mass of Si/RGO-AG. The initial discharge/charge capacities were 3446 and 2535 $mAh \cdot g^{-1}$, respectively, to give an initial coulombic efficiency of 73.6 %. The initial irreversible capacity of electrode Si/RGO-AG can be attributed to the formation SEI, the unexpected reaction of the remaining oxygen-containing groups in the RGO aerogel and SiO_2 layer on the surface of SiNPs with Li ions. [27, 38] After the second cycle, the coulombic efficiency tended to increase and stabilize. It is interesting to note that the curves of the second and third cycles almost overlapped each other, which indicates a good cycling stability of the electrode. The reversible capacities of the second and third cycles compared with the first cycle were slightly increased, which can be attributed to the activation of the SiNPs in the Si/RGO-AG composite.

Figure 3C shows the cycling performance of Si/RGO-AG at a current density of 150 $mA \cdot g^{-1}$, together with electrodes Si/RGO-SWAG and Si/RGO. It can be seen that the initial charge and discharge capacities of electrode Si/RGO were the lowest among the three electrodes studied. This poor performance of electrode Si/RGO was probably due to severe aggregation of the SiNPs, indicating the RGO sheets did not stabilize the SiNPs well. After about 20 cycles, the reversible capacity dropped drastically to about 450 $mAh \cdot g^{-1}$, confirming that the SiNPs were not stabilized well by the RGO

sheets. These results suggest that the physical mixing method is not a good approach to stabilizing SiNPs. While the initial discharge/charge capacities of electrode Si/RGO-SWAG reached to 3360 and 2450 mAh·g^{-1}, respectively, its reversible capacity decreased to about 615 mAh·g^{-1} after 40 cycles. The improved performance of electrode Si/RGO-SWAG indicates the single-step wrapping method illustrated in Scheme 1 is advantageous over the physical mixing method. This fast capacity fading however indicates that the single-step wrapping method still could not afford efficient stabilization of SiNPs. On contrast, the Si/RGO-AG electrode showed a significantly improved cycling performance with the highest initial charge/discharge capacities and delivered a reversible capacity of 1984 mAh·g^{-1} after 40 cycles.

Figure 3D demonstrates the rate capability of the Si/RGO-AG at current densities ranging from 170 mA·g^{-1} to 2500 mA·g^{-1}. The battery delivered a reversible capacity of about 1000 and 600 mAh·g^{-1} at the current densities of 2000 and 2500 mA·g^{-1}, respectively. Furthermore, the capacity reached around 2000 mAh·g^{-1} when the current density was decreased to 170 mA·g^{-1} after having been cycled at higher current densities, indicating a good cycling stability of Si/RGO-AG.

Figure S7A shows the SEM image of electrode Si/RGO-AG after 40 cycles. As can be seen, the Si/RGO-AG composite maintained its integrity and porous structure. In addition, the SiNPs were entrapped by the RGO framework, contributing to the significantly improved cycling performance of Si/RGO-AG. The Nyquist plots of the Si/RGO-AG electrode are presented in Figure S7B. The depressed semicircle in the high-frequency region represents the resistance of the SEI film and the charge-transfer resistance, while the straight lines in the low-frequency region corresponds to the diffusion kinetics of lithium ions. No obvious impedance increase is observed after cycling due to the stable SEI. The impedance decrease may be attributed to the gradual electrolyte transport into the electrode and the increasing conductivity of the SiNPs after lithiation.

The improved cycle performance and enhanced rate capability of Si/RGO-AG can be attributed to the following reasons: i) the Si/RGO-AG composite created sufficient space and efficiently accommodated the drastic volume change of the entrapped SiNPs during cycling; ii) the interconnected 3D RGO aerogel network maintained the integrity of the electrode structure, prohibited the detachment of the SiNPs from the current collector and improved the electrical conductivity of the electrode; iii) the existence of meso- and macro- pores provided an efficient pathway for electrolyte transport and facilitated Li^+ diffusion, thus enhancing the rate performance.

Conclusions

In conclusion, we have demonstrated an approach to preparing a high-performance LIB negative electrode material by encapsulating SiNPs in 3D RGO aerogel. The RGO aerogel with a porous network offers space for accommodating SiNPs, as well as facilitating electron and electrolyte transport. The composite electrode delivered a stable cycling performance with a capacity of about 2000 mA h g^{-1} after 40 cycles, together with an excellent rate capability.

Acknowledgements

The authors would like to thank the Australia Research Council (ARC) for funding this work under projects FT100100879 and DP130101870. The facilities and technical assistance of the Australian Microscopy and Microanalysis Research Facility at the Centre for Microscopy and Microanalysis at The University of Queensland are acknowledged. The author also specially thanks the China Scholarship Council.

[a] School of Chemical Engineering, The University of Queensland, St. Lucia, Brisbane, QLD 4072, Australia.
Email: george.zhao@uq.edu.au
[b] School of Chemical Engineering and Technology, Harbin Institute of Technology, Xidazhi Street, 150001 Harbin, China.
[c] Materials Engineering, The University of Queensland, St. Lucia, Brisbane, QLD 4072, Australia.
Electronic Supplementary Information (ESI) available: [details of any supplementary information available should be included here]. See DOI: 10.1039/c000000x/

References

1 B. Scrosati and J. Garche, *J. Power Sources*, 2010, **195**, 2419-2430.
2 U. Kasavajjula, C. Wang and A. J. Appleby, *J. Power Sources*, 2007, **163**, 1003-1039.
3 C. M. Park, J. H. Kim, H. Kim and H. J. Sohn, *Chem. Soc. Rev.*, 2010, **39**, 3115-3141.
4 N. Liu, H. Wu, M. T. McDowell, Y. Yao, C. Wang and Y. Cui, *Nano Lett.*, 2012, **12**, 3315-3321.
5 X. Su, Q. Wu, J. Li, X. Xiao, A. Lott, W. Lu, B. W. Sheldon and J. Wu, *Adv. Energy Mater.*, 2014, **4**, 1-23.
6 J. R. Szczech and S. Jin, *Energy Environ. Sci.*, 2011, **4**, 56-72.
7 B. Scrosati, J. Hassoun and Y. K. Sun, *Energy Environ. Sci.*, 2011, **4**, 3287-3295.
8 X. S. Zhou, Y. X. Yin, L. J. Wan and Y. G. Guo, *Chem. Commun.* , 2012, **48**, 2198-2200.
9 J. K. Lee, K. B. Smith, C. M. Hayner and H. H. Kung, *Chem. Commun.* , 2010, **46**, 2025-2027.
10 S. N. Yang, G. R. Li, Q. Zhu and Q. M. Pan, *J. Mater. Chem.* , 2012, **22**, 3420-3425.
11 L. F. Cui, R. Ruffo, C. K. Chan, H. Peng and Y. Cui, *Nano Lett.*, 2008, **9**, 491-495.
12 L. F. Cui, Y. Yang, C. M. Hsu and Y. Cui, *Nano Lett.*, 2009, **9**, 3370-3374.
13 M. T. McDowell and Y. Cui, *Adv. Energy Mater.*, 2011, **1**, 894-900.
14 H. T. Nguyen, F. Yao, M. R. Zamfir, C. Biswas, K. P. So, Y. H. Lee, S. M. Kim, S. N. Cha, J. M. Kim and D. Pribat, *Adv. Energy Mater.*, 2011, **1**, 1154-1161.
15 W. L. Xu, S. S. S. Vegunta and J. C. Flake, *J. Power Sources*, 2011, **196**, 8583-8589.
16 Y. Yao, M. T. McDowell, I. Ryu, H. Wu, N. A. Liu, L. B. Hu, W. D. Nix and Y. Cui, *Nano Lett.*, 2011, **11**, 2949-2954.
17 M. H. Park, M. G. Kim, J. Joo, K. Kim, J. Kim, S. Ahn, Y. Cui and J. Cho, *Nano Lett.*, 2009, **9**, 3844-3847.
18 L. W. Su, Z. Zhou and M. M. Ren, *Chem. Commun.* , 2010, **46**, 2590-2592.
19 Y. Chen, C. Li, Y. G. Wang, Q. Zhang, C. Y. Xu, B. Q. Wei and L. N. An, *J. Mater. Chem.* , 2011, **21**, 18186-18190.
20 M. K. Datta, J. Maranchi, S. J. Chung, R. Epur, K. Kadakia, P. Jampani and P. N. Kumta, *Electrochim. Acta* 2011, **56**, 4717-4723.

21 Y. H. Xu, G. P. Yin, X. Q. Cheng and P. J. Zuo, *Electrochim. Acta* 2011, **56**, 4403-4407.
22 Y. X. Yin, S. Xin, L. J. Wan, C. J. Li and Y. G. Guo, *J. Phys. Chem. C*, 2011, **115**, 14148-14154.
23 X. S. Zhou, Y. X. Yin, L. J. Wan and Y. G. Guo, *Adv. Energy Mater.*, 2012, **2**, 1086-1090.
24 C. Xu, B. Xu, Y. Gu, Z. Xiong, J. Sun and X. Zhao, *Energy Environ. Sci.*, 2013, **6**, 1388-1414.
25 B. Wang, X. Li, X. Zhang, B. Luo, M. Jin, M. Liang, S. A. Dayeh, S. Picraux and L. Zhi, *Acs Nano*, 2013, **7**, 1437-1445.
26 X. Zhao, C. M. Hayner, M. C. Kung and H. H. Kung, *Adv. Energy Mater.*, 2011, **1**, 1079-1084.
27 H. F. Xiang, K. Zhang, G. Ji, J. Y. Lee, C. J. Zou, X. D. Chen and J. S. Wu, *Carbon*, 2011, **49**, 1787-1796.
28 W. Chen and L. Yan, *Nanoscale*, 2011, **3**, 3132-3137.
29 Z.-S. Wu, S. Yang, Y. Sun, K. Parvez, X. Feng and K. Müllen, *J. Am. Chem. Soc.*, 2012, **134**, 9082-9085.
30 W. Chen, S. Li, C. Chen and L. Yan, *Adv. Mater.* , 2011, **23**, 5679-5683.
31 S.-H. Park, H.-K. Kim, D.-J. Ahn, S.-I. Lee, K. C. Roh and K.-B. Kim, *Electrochem. Commun.* , 2013, **34**, 117.
32 Z. G. Xiong, L. L. Zhang, J. Z. Ma and X. S. Zhao, *Chem. Commun.* , 2010, **46**, 6099-6101.
33 V. Kesler, S. Yanovskaya, G. Kachurin, A. Leier and L. Logvinsky, *Surf. Interface Anal.*, 2002, **33**, 914-917.
34 S. Sim, P. Oh, S. Park and J. Cho, *Adv. Mater.* , 2013, **25**, 4498-4503.
35 J. Z. Wang, C. Zhong, S. L. Chou and H. K. Liu, *Electrochem. Commun.* , 2010, **12**, 1467-1470.
36 X. Zhang, Z. Sui, B. Xu, S. Yue, Y. Luo, W. Zhan and B. Liu, *J. Mater. Chem.* , 2011, **21**, 6494-6497.
37 Y. Zhu, W. Liu, X. Zhang, J. He, J. Chen, Y. Wang and T. Cao, *Langmuir*, 2013, **29**, 744-749.
38 J. Deng, H. Ji, C. Yan, J. Zhang, W. Si, S. Baunack, S. Oswald, Y. Mei and O. G. Schmidt, *Angew. Chem.*, 2013, **125**, 2382-2386.

Table of contents

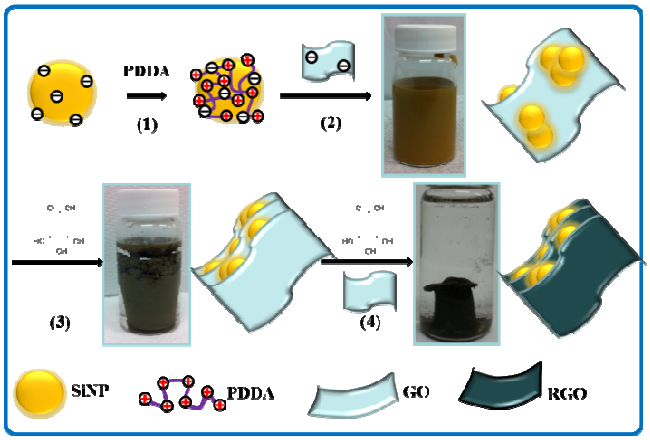

Scheme 1. Schematic illustration of the preparation of Si/RGO-AG: 1) surface modification of SiNPs with PDDA; 2) formation of Si@GO composite via electrostatic interactions; 3) reduction of Si@GO using GA to form Si@RGO hydrogel; 4) dispersing Si@RGO in a GO suspension for further reduction using GA.